Supporting Information for

Mantle exhumation and post-rift magmatism at an oblique magma-poor continental margin

Jie Chen[1,2,3], Sylvie Leroy[2], Louise Watremez[4], Adam H. Robinson[5]

[1] Université Paris Cité, Institut de physique du globe de Paris, 75005 Paris, France

[2] Sorbonne Université, CNRS-INSU, Institut des Sciences de la Terre Paris, 75005, Paris, France

[3] Laboratoire de Géologie, Ecole Normale Supérieure, PSL Research University, Paris 75005, France

[4] Université de Lille, CNRS, Université Littoral Côte d'Opale, IRD, UMR 8187, Laboratoire d'Océanologie et de Géosciences, Lille, France

[5] School of Ocean and Earth Science, University of Southampton, Southampton, UK

Corresponding author: Jie Chen (chen@geologie.ens.fr)

This PDF file includes:

- Text S1
- Fig. S1-S15
- Table S1-S3
- References

Text S1

Data acquisition

The 3-D wide-angle seismic refraction data used in this paper were collected by a combined onshore-offshore survey during the Encens cruise in 2006 (Leroy, 2006; Leroy et al., 2010; Watremez et al., 2011), and comprise ~7500 offshore air-gun shots along 15 track lines (1110 km in total) with a shot interval of ~150 m (60 s at a speed of ~5 knots). The source is made up of an array of 18 air guns with a total volume of 138 L, towed at 22–25 m depth. The data were recorded by 35 ocean-bottom seismometers (OBS) deployed at intervals of 10-15 km and 13 land seismometers (Fig. 1C). The internal clocks of the OBSs were synchronized with a linear drift correction during deployment and recovery, and the OBS positions were relocated to their true position on the seafloor by the inversion of the direct wave arrival times (Watremez et al., 2011).

Traveltime Picking

P-wave first arrival traveltimes are picked from the vertical component and the hydrophone of the receivers (e.g., Fig. S1; note that land stations only have the vertical component). Approximately 180 000 first arrivals are picked within shot-receiver offsets up to 140 km for OBSs and 190 km for land seismometers (Fig. S2A). To account for errors of picking and instrument location, uncertainties are artificially assigned to traveltime picks based on the shot-receiver offset, which are 20, 50, 80, 100, and 150 ms for offsets at 0-5, 5-10, 10-20, 20-50, and >50 km, respectively (Table S1).

Setup for seismic tomography in FAST

Travel times were inverted in 3-D using the FAST (First-Arrival Seismic Tomography), which applies a regularized inversion method to iteratively construct a smooth 3-D velocity model (Zelt & Barton, 1998). The parameters used in the inversions are summarized in Table S2 (Zelt & Barton, 1998). Each starting model is inverted with 10 iterations and 6 values of the trade-off parameter (λ). The model space has dimensions of 215 × 155 × 37 km in X (-5 to 210 km), Y (-5 to 150 km), and Z (-2 to 35 km below sea level). The node spacing is 0.5 km both laterally and vertically for the forward grid, and 1 km laterally and 0.5 km vertically for the inverse grid. In the oceanic domain, the seafloor is constructed from the shipboard bathymetry data, and the sediment thickness is constructed using multichannel seismic reflection data (Autin et al., 2010; d'Acremont et al., 2005). The land topography is constructed using the GEBCO database (Weatherall et al., 2015).

Starting 3-D velocity model

The starting 3-D P-wave velocity (Vp) model is composed of separate velocity profiles for the oceanic and terrestrial domains (Fig. S3), with a straight boundary to represent the simplified COT, here referred to as continent-ocean boundary (COB). An example is shown in Fig. S3. In the oceanic domain, the Vp is fixed in the water layer at 1.5 km/s, and linearly increases from 1.6 to 4 km/s in the sediment layer and from 4 to 7.5 km/s from the basement top to the Moho (Fig. S3F). The Moho (defined as 7.5 km/s) is located at 6 km (i.e., crustal thickness) below the basement top. For the terrestrial domain, (north to the coast in Fig. S3a), the starting model linearly increases from 4 km/s at the surface to 7.5 km/s at the Moho (Fig. S3e). The upper mantle has a thickness of 3 km with Vp linearly increasing from 7.5 to 8 km/s. Vp at the base of the model is 8.2 km/s. The COB location is inferred from previous 2-D seismic tomography (Leroy et al., 2010; Watremez et al., 2011), corresponding to a velocity gradient towards the terrestrial domain with ΔY (90 km) and ΔZ (15 km) (e.g., Fig. S3D).

Monte-Carlo analysis

We apply a Monte-Carlo analysis (Korenaga et al., 2000), in order to determine the uncertainty on calculated velocities and to test any issues which may relate to final model dependence on the choice of starting model. A set of 100 starting velocity models are created by perturbing each starting model parameter within the ranges given in Table S3. In addition, we add random noise to the picked first arrival traveltimes (Watremez et al., 2015; Zhang & Toksöz, 1998), linking to 1) instrumental uncertainties with the maximum value of ±62.5 ms and 2) picking uncertainties with a Gaussian distribution scaled according to the assigned uncertainties, which yields a set of 100 synthetic traveltime data sets.

100 random combinations of starting velocity models and synthetic traveltimes are inverted as above, with the final model of each inversion chosen as the iteration when $\chi^2 \approx 1$. The 100 final models are averaged, and the velocity standard deviation is calculated (Fig. S7). Traveltime residuals of the final model do not show any significant dependence on receivers or shot-receiver offsets (Fig. S2), with only slightly higher residuals at land stations.

Checkerboard test and model resolution

To assess the spatial resolution of the final velocity model, we perform a set of checkerboard tests (Fig. S13-S14), following the previous approach (Zelt, 1998). An alternating polarity, cubic checkerboard pattern with velocity perturbation ±5% is applied to the final velocity model. Synthetic traveltimes are calculated by forward ray tracing using the shot-receiver geometries, and random noise is added proportionately to the instrumental and picking uncertainties. These resulting travel times are then re-inverted to recover the checkerboard pattern. 9 different checkerboard cell sizes are tested, from 4 to 20 km at 2 km intervals (Fig. S14). Each cell size has 8 different patterns with spatially shifting of 0, 0.5, 1, and 1.5 of the cell size in all three directions, as well as horizontally rotating of 0° and 45° (e.g., Fig. S13A-S13H for the checkerboard of the cell size at 10 km) in order to reduce potential effects of preferential ray-path or checkerboard null-plane alignments. Resolvability is represented as the semblance, calculated using an operator radius the same as the checkerboard cell size. Semblance is averaged across lateral shifts and rotations for each checkerboard size (Fig. S14). A semblance of ≥0.7 is considered as well resolved (Zelt, 1998). For lower cell sizes and shallower depths, the semblance is higher and thus the lateral resolution is also higher (Fig. S14). The model surrounding the COT exhibits a good spatial resolution at Z≤12 km with a cell size of 10 km (Fig. S14).

We combine all areas of semblance of 0.7 for 9 different cell sizes and interpolate them to generate a map of spatial resolution (Fig. S8 and S11). The higher ray density at the central and shallow part of the model enables a better resolution, while the deep part and the edge of the model have the lowest spatial resolution due to the lack of ray coverage (Fig. S6 and S8).

Comparing with previous 2-D Vp tomography

We compare our results of the 3-D Vp tomography model with previous co-incident 2-D Vp tomography models (Fig. S15) (Leroy et al., 2010; Watremez et al., 2011). 8 velocity profiles (L1-L5 and L7-L9) were constructed in 2-D using Ranvir, which includes both first arrivals, and reflections from the top of the oceanic basement and the Moho (PmP) (Watremez et al., 2011). This modelling approach includes sharp interfaces at the e.g., oceanic basement and the Moho, which cannot be modelled using the FAST inversion approach. The location of the Moho in the 2-D profiles is comparable to the 7.5 km/s iso-velocity contour in our 3-D model, especially at the COT and the oceanic crust (e.g., L2 in Fig. S15A-2 and L5 in Fig. S15C-1), suggesting that this velocity in our model represents a good proxy of the Moho location. The difference between the Moho in the 2-D and the 7.5 km/s iso-velocity in 3-D is larger in the continental domain (e.g., L2 in Fig. S15A-2, L3 in Fig. S15B-1, L8 in Fig. S15D-2, and L9 in Fig. S15D-3), probably due to the lack of the rays in both models. The crustal thickness in the continental domain of our model is not considered as well defined. Besides, both 2-D and the 3-D models have a good agreement in imaging small-scale Vp features in the shallow region (<5 km below the seafloor), e.g., the spur-shaped basement structure at X=52 km of profile L4 (Fig. S15B-2) and seamounts at X=31 km of profile L2 (Fig. S15A-2).

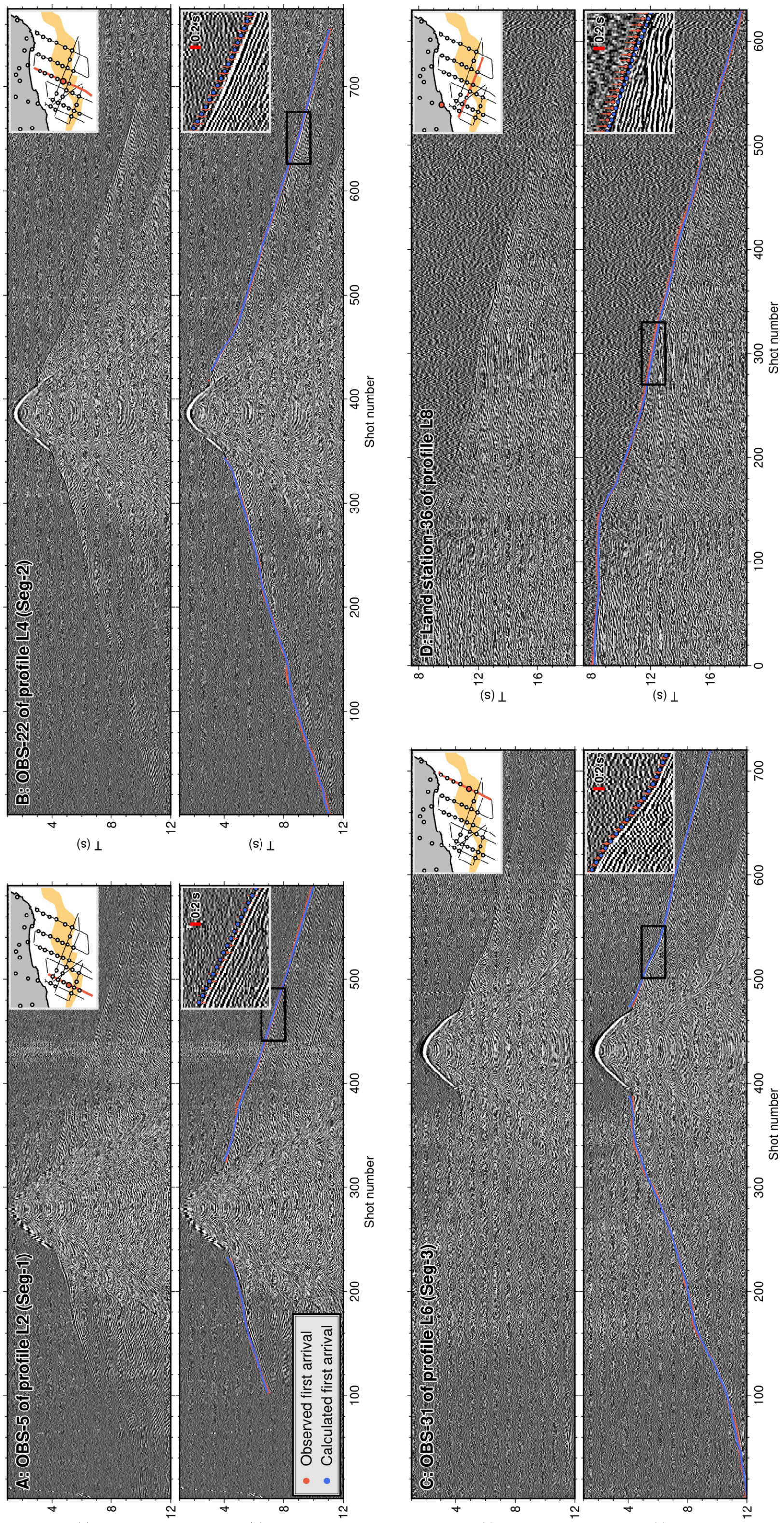

Figure S 1. **Examples of seismic records.** No reduction or filter is applied. Upper panels: uninterpreted seismic records. The inset maps show the location of the shot track (red line) and OBS or land station (red circle). Lower panels: interpreted seismic records with observed (red dots with uncertainties) and calculated (blue dots) first arrivals. The inset is the close-up within the black rectangle. Red bar is the time scale of 0.2 s.

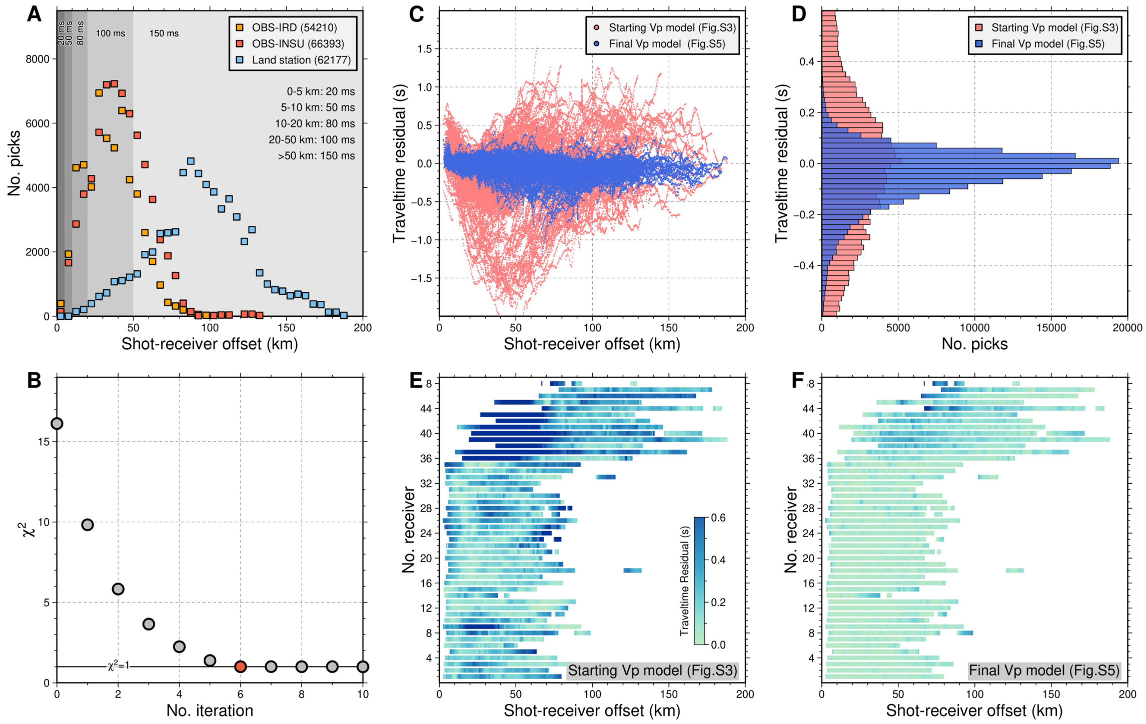

Figure S 2. **3-D model travel-time fit analysis.** (**A**) First-arrival picking number recorded by OBSs and land stations. Shot-receiver offset dependent picking uncertainties are indicated. (B) Reduction of the χ^2 with respect to the number of iterations in FAST, using the starting Vp model in Fig. S3. The inverted Vp model with $\chi^2 \approx 1$ at end of iteration 6 (red circle) is chosen for the final model. (C) and (D) Traveltime residuals of the starting Vp model in Fig. S3 (pink) and the final Vp model (blue, average of 100 Monte-Carlo final models). (E) and (F) Traveltime residuals for each receiver binned at 0.5 km source-receiver offset intervals for the starting Vp model in Fig. S3 and the final Vp model, respectively.

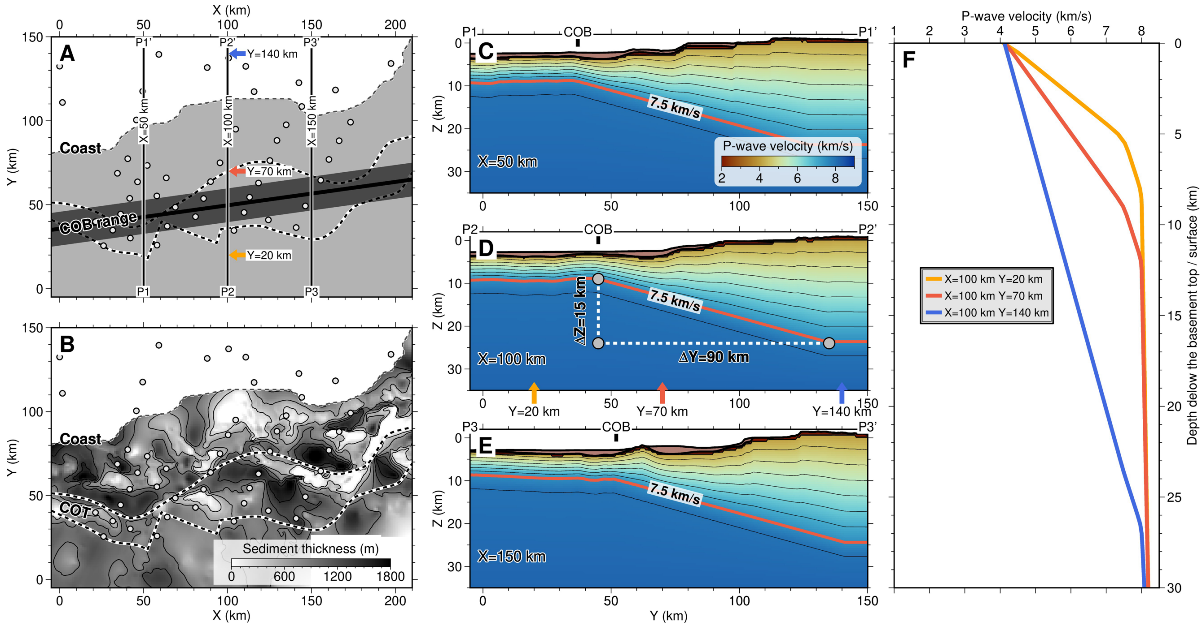

Figure S 3. **Central case of starting Vp models, with parameters in the middle of the ranges of the Monte-Carlo analysis.** (**A**) Simplified structural map showing the coast, the COT (dashed contour), and a simplified continent-ocean boundary (COB) and its range (shaded area). (**B**) Map of sediment thickness (Autin et al., 2010; d'Acremont et al., 2005). (**C**) - (**E**) Vertical Vp slices through the central case of starting Vp models along profiles P1-P1', P2-P2', and P3-P3'. The COB used in this starting model is shown as the black solid line in Fig. S3A. The contour interval is 0.5 km/s. The slope of the 7.5 km/s iso-velocity, to the north of the COB, is defined by ∆Y (90 km) and ∆Z (15 km) based on previous 2-D seismic tomography (Leroy et al., 2010; Watremez et al., 2011). (**F**) Three 1-D Vp profiles of the P2-P2' profile represent the oceanic crust (orange line), the COT crust (red line), and the continental crust (blue line).

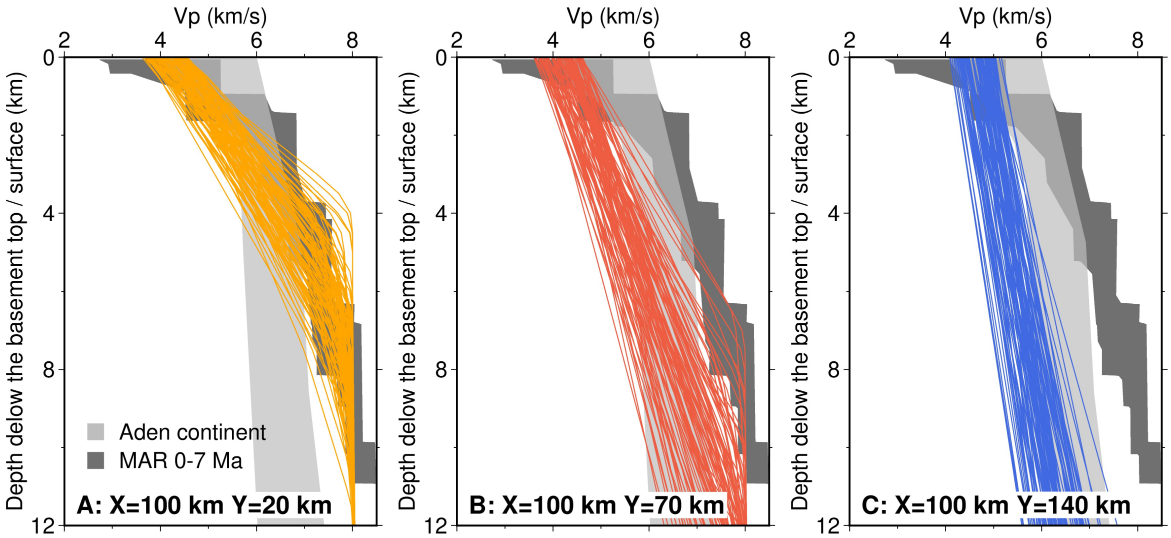

Figure S 4. **1-D Vp starting models, extracted from 100 random 3-D starting Vp models in Monte-Carlo analysis.** (**A**), (**B**), and (**C**) represent oceanic, COT, and continental crusts, respectively; their locations are shown as arrows with the same color in the P2-P2' profile of Fig. S3A. Velocity envelopes in black and gray represent the oceanic crust of the Mid-Atlantic Ridge (MAR) (White et al., 1992) and the continental crust of the north-eastern Gulf of Aden (Leroy et al., 2010; Watremez et al., 2011), respectively.

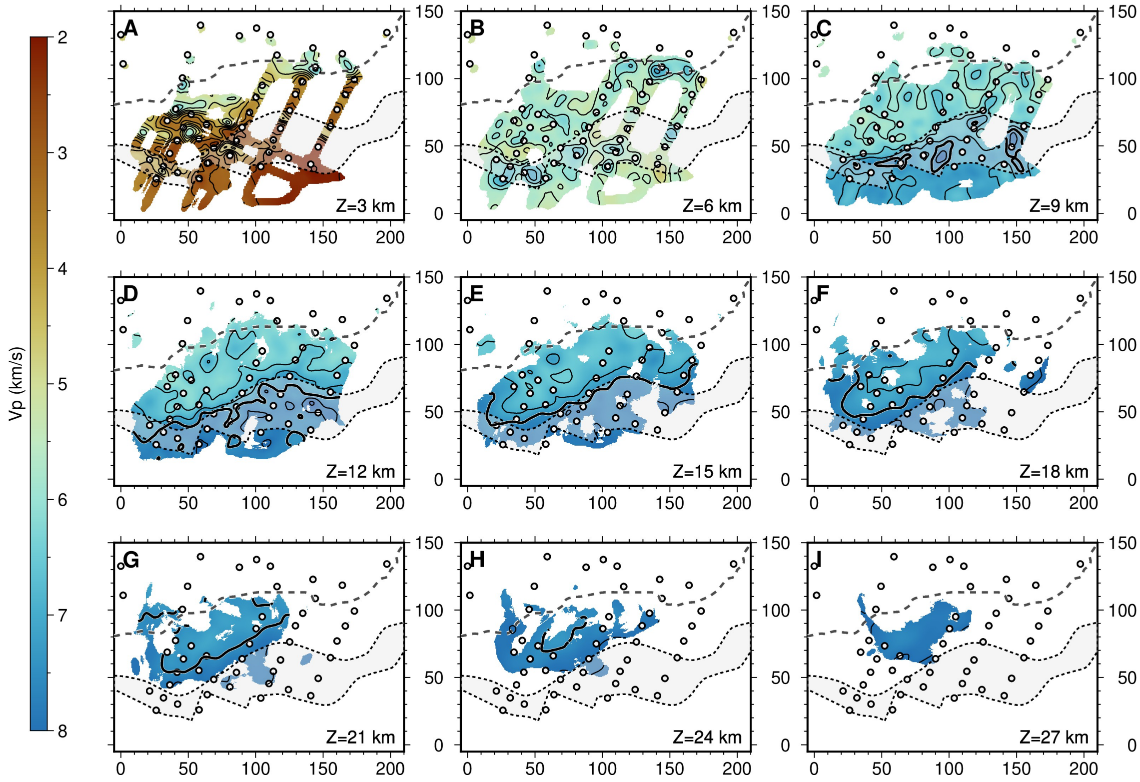

Figure S 5. **Depth slices (below the sea level) through the final Vp model.** White masks correspond to areas without ray coverage. Contour interval is 0.5 km/s, highlighting the 7.5 km/s. Coast and COT are plotted as dashed line and gray shaded area, respectively.

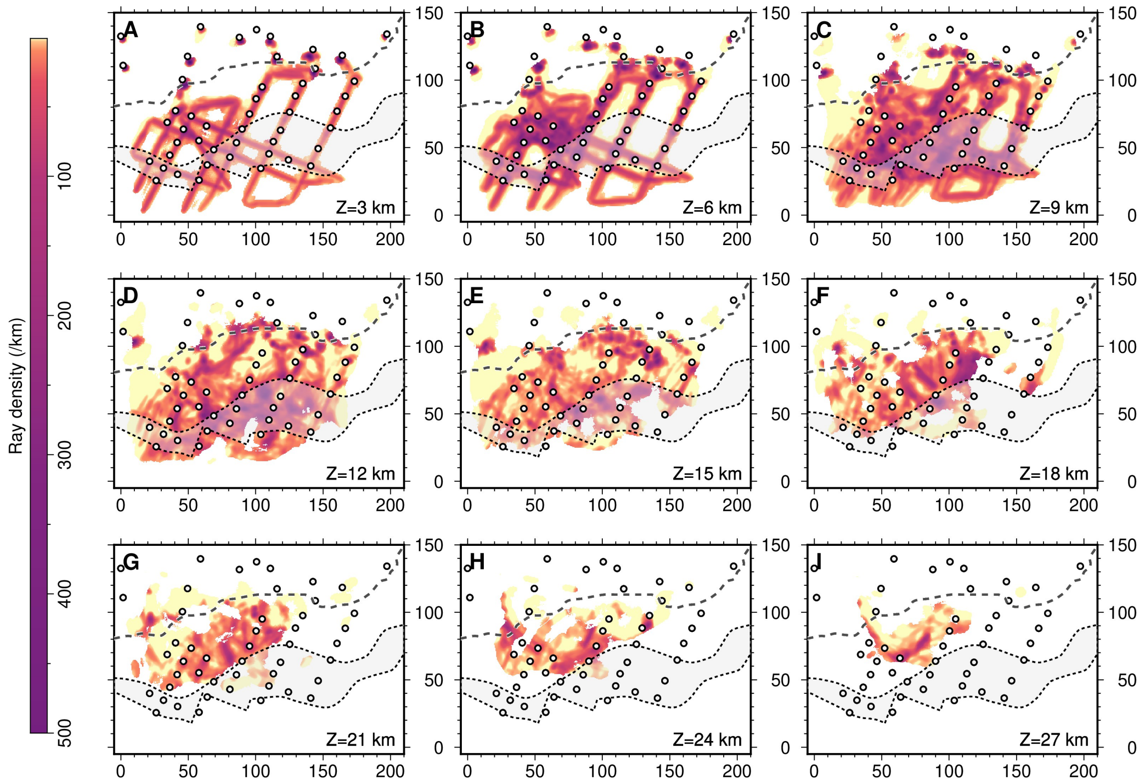

Figure S 6. **Depth slices of ray density through the final Vp model.** Symbols are identical to Fig. S5.

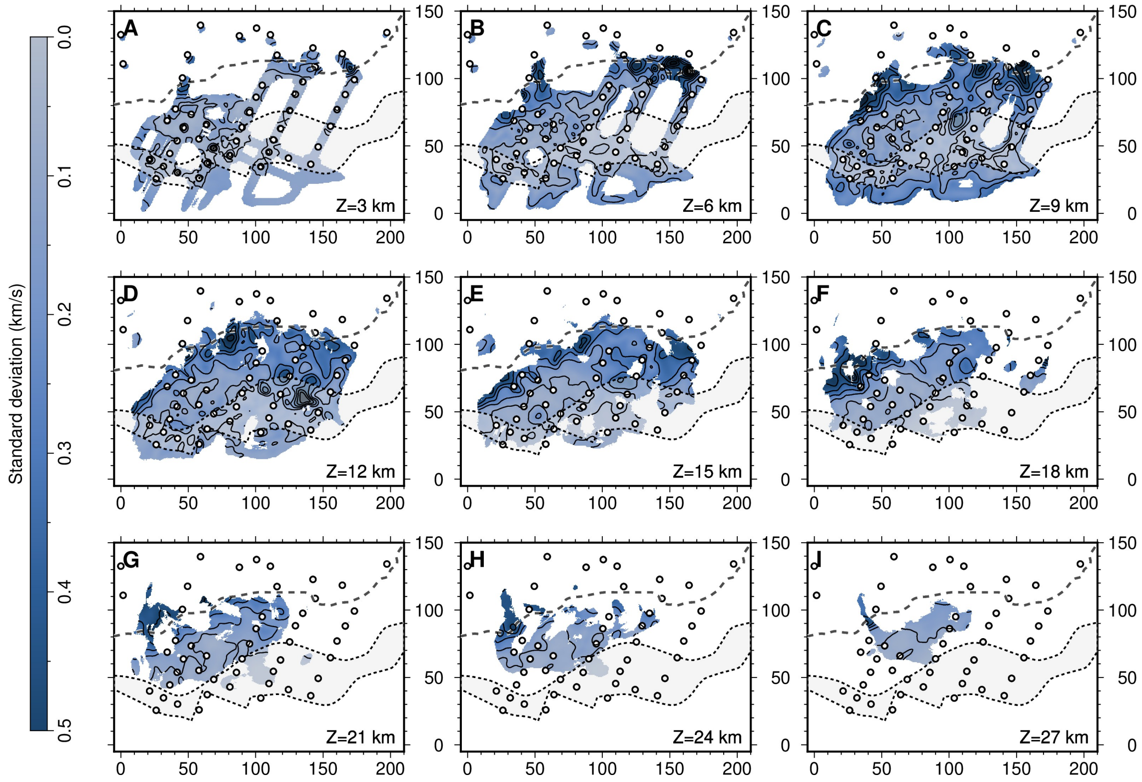

Figure S 7. **Depth slices of standard deviation of 100 Monte-Carlo final Vp models.** The contour interval is 0.1 km/s. Symbols are identical to Fig. S5.

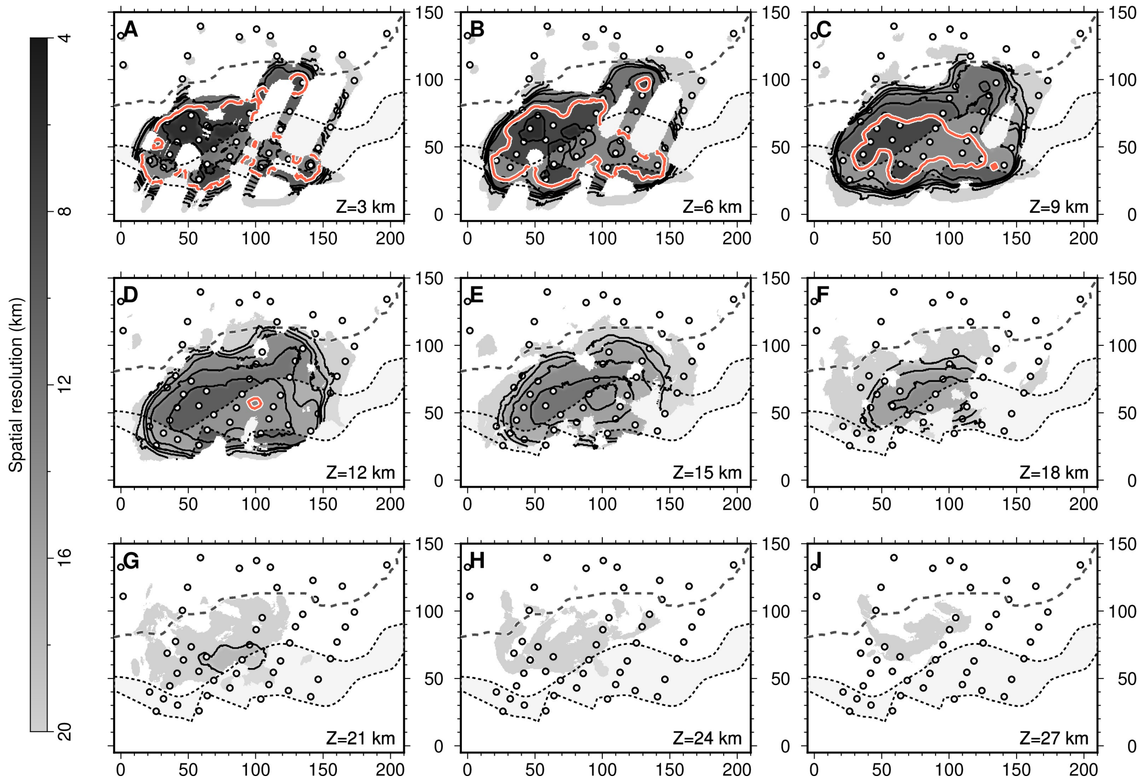

Figure S 8. **Depth slices of spatial resolution, based on the minimum cell size in checkerboard test with semblance>0.7**. Contour interval is 2 km, highlighting the 10 km (in red). Symbols are identical to Fig. S5.

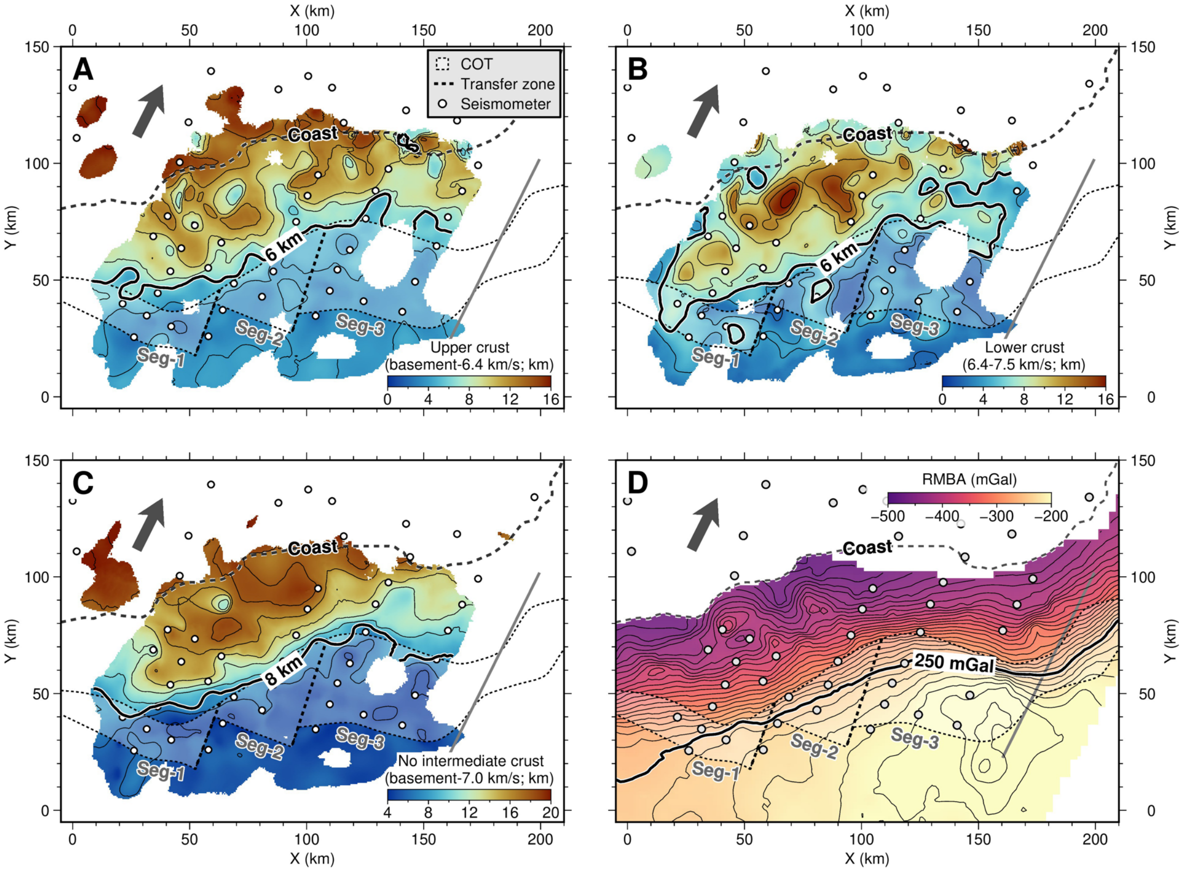

Figure S 9. **Map view of the final Vp model and RMBA.** White masks correspond to areas without ray coverage. Gray arrows show the extension direction. (**A**) Upper crustal thickness, calculated between the basement top and the 6.4 km/s iso-velocity. Contour interval is 2 km, highlighting the 6 km. (**B**) Lower crustal thickness, calculated between the 6.4 and the 7.5 km/s iso-velocities. Contour interval is 2 km, highlighting the 6 km. (**C**) Crustal thickness without the intermediate velocity, calculated between the basement top and the 7.5 km/s iso-velocity. Contour interval is 2 km, highlighting the 8 km. (**D**) Residual mantle bouguer gravity anomaly (RMBA) (d'Acremont et al., 2010). Contour interval is 10 mGal, highlighting the 250 mGal.

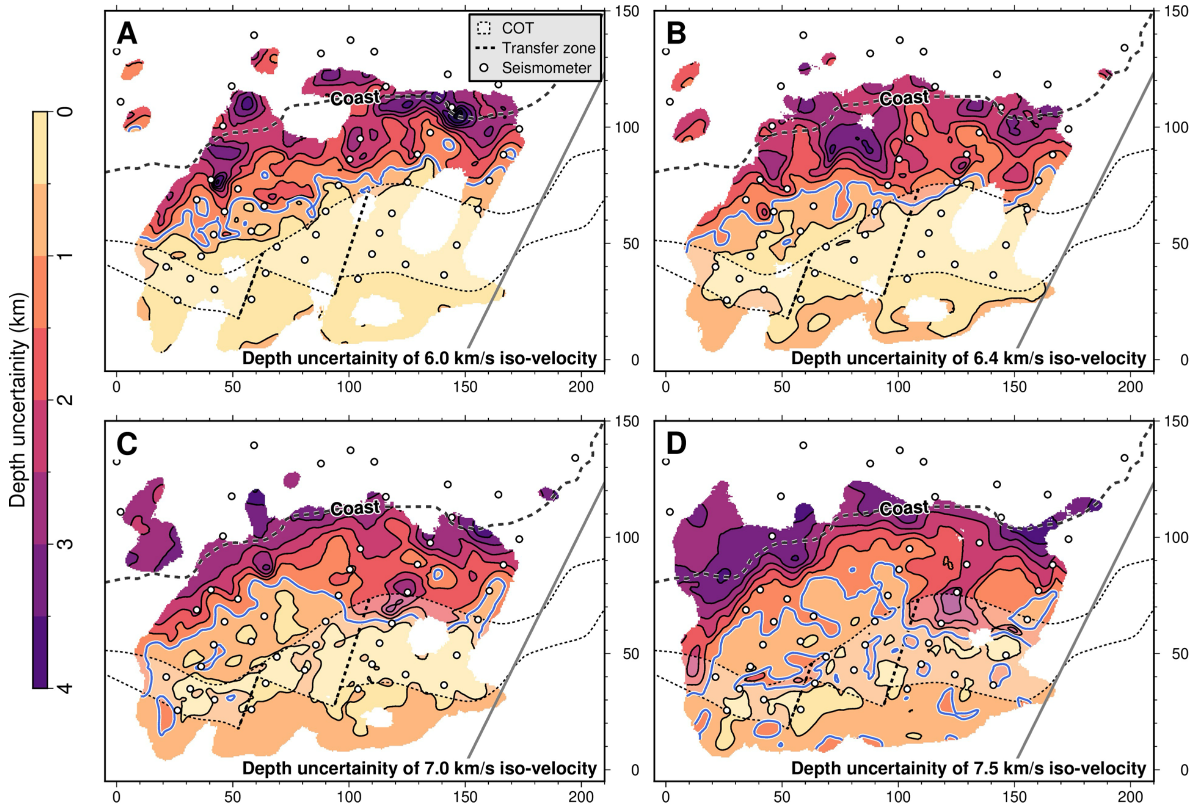

Figure S 10. **Map view of depth uncertainties of iso-velocities at 6.0 km/s (A), 6.4 km/s (B), 7.0 km/s (C), and 7.5 km/s (D)**, derived from the standard deviation of 100 Monte-Carlo final Vp models. White masks correspond to areas without ray coverage. Contour interval is 0.5 km, highlighting the 1 km (in blue).

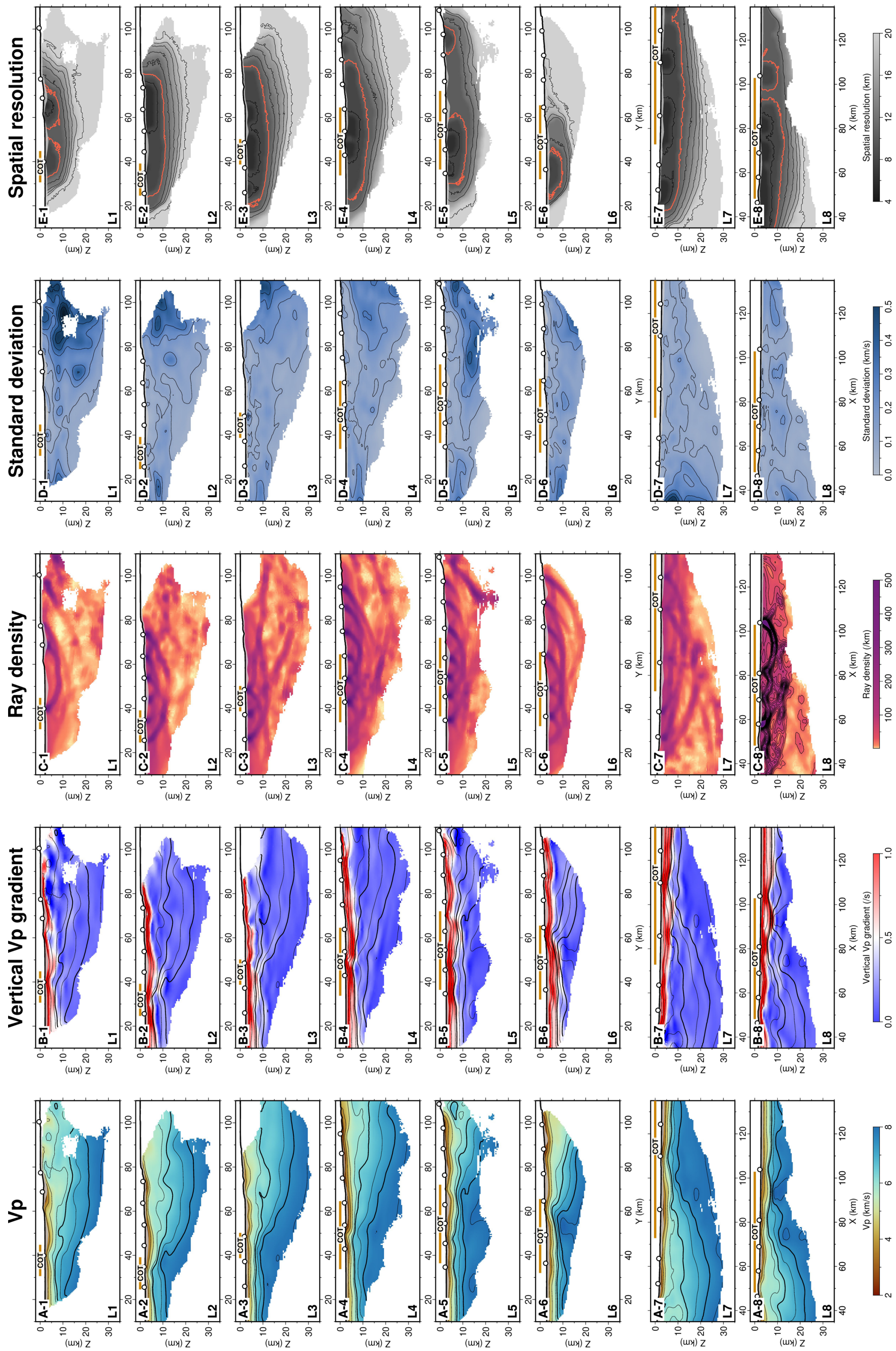

Figure S 11. **Vertical slices of Vp (A), vertical Vp gradient (B), ray density (C), standard deviation of 100 Monte-Carlo final Vp models (D), and spatial resolution (E).** Locations of 8 profiles (L1-L8) are shown in Fig. 2A.

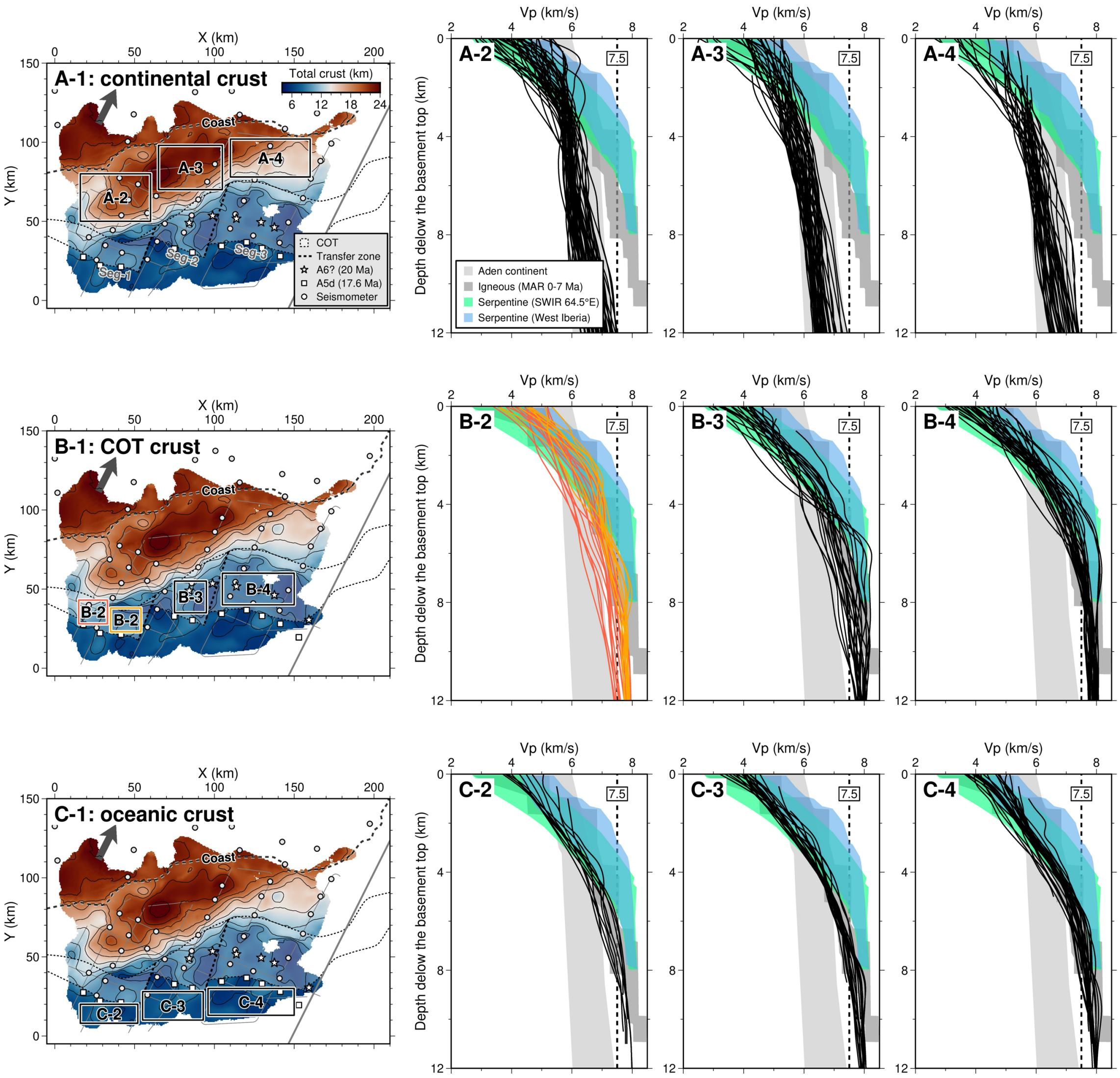

Figure S 12. **1-D Vp profiles of continental (A), COT (B), and oceanic (C) crusts.** 1-D profiles are sampled with an interval of 5 km in both X and Y directions, within the corresponding boxes in A-1, B-1, and C-1 that are crustal thickness map in Fig. 2B. Velocity envelopes in light and dark gray represent the continental crust of the north-eastern Gulf of Aden (Leroy et al., 2010; Watremez et al., 2011) and the igneous crust of the MAR 0-7 Ma (White et al., 1992), respectively. Green and blue envelopes represent serpentinized mantle of the ultraslow spreading SWIR 64.5°E (Corbalán et al., 2021; Momoh et al., 2017) and the magma-poor West Iberia rifted margin (Davy et al., 2016), respectively. Note that red and orange boxes in B-1 show the locations of corresponding colored 1-D profiles in B-2.

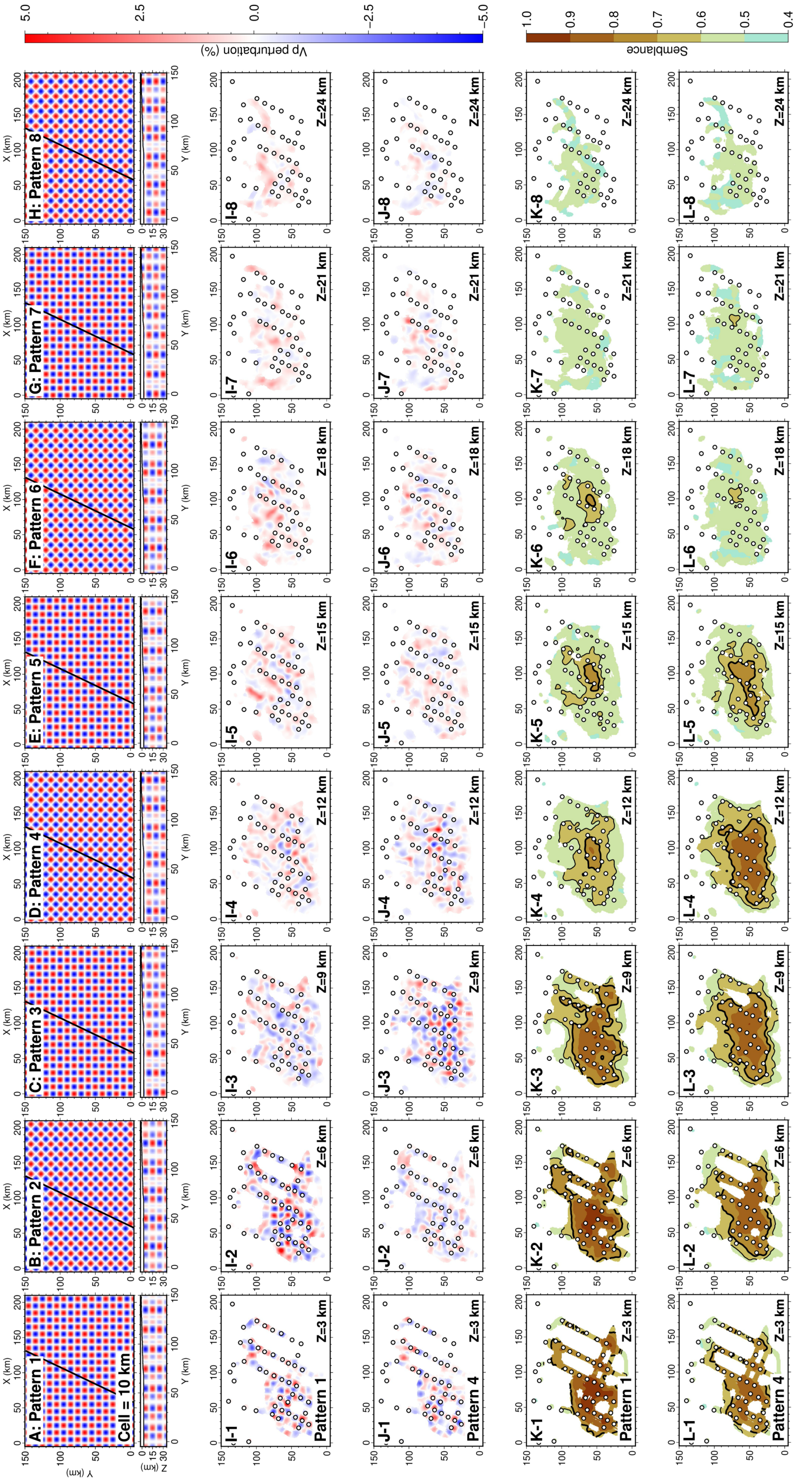

Figure S 13. **Checkerboard tests with cell size of 10 km.** (**A**) - (**H**) 8 different input pattens with shifting of 0, 0.5, 1, and 1.5 of the cell size in X, Y, and Z directions, and rotations of 0° and 45°. Lower panels show vertical slices along black line in upper panels. (**I**) and (**K**) Semblance of Pattern 1 at different depths, with no shifting or rotation of the input pattern. Contours of the semblance of 0.6 (thin line) and 0.7 (thick line) are plotted. (**J**) and (**L**) Semblance of Pattern 4, with shifts of 0.5 of the cell size and 45° rotation applied to input pattern.

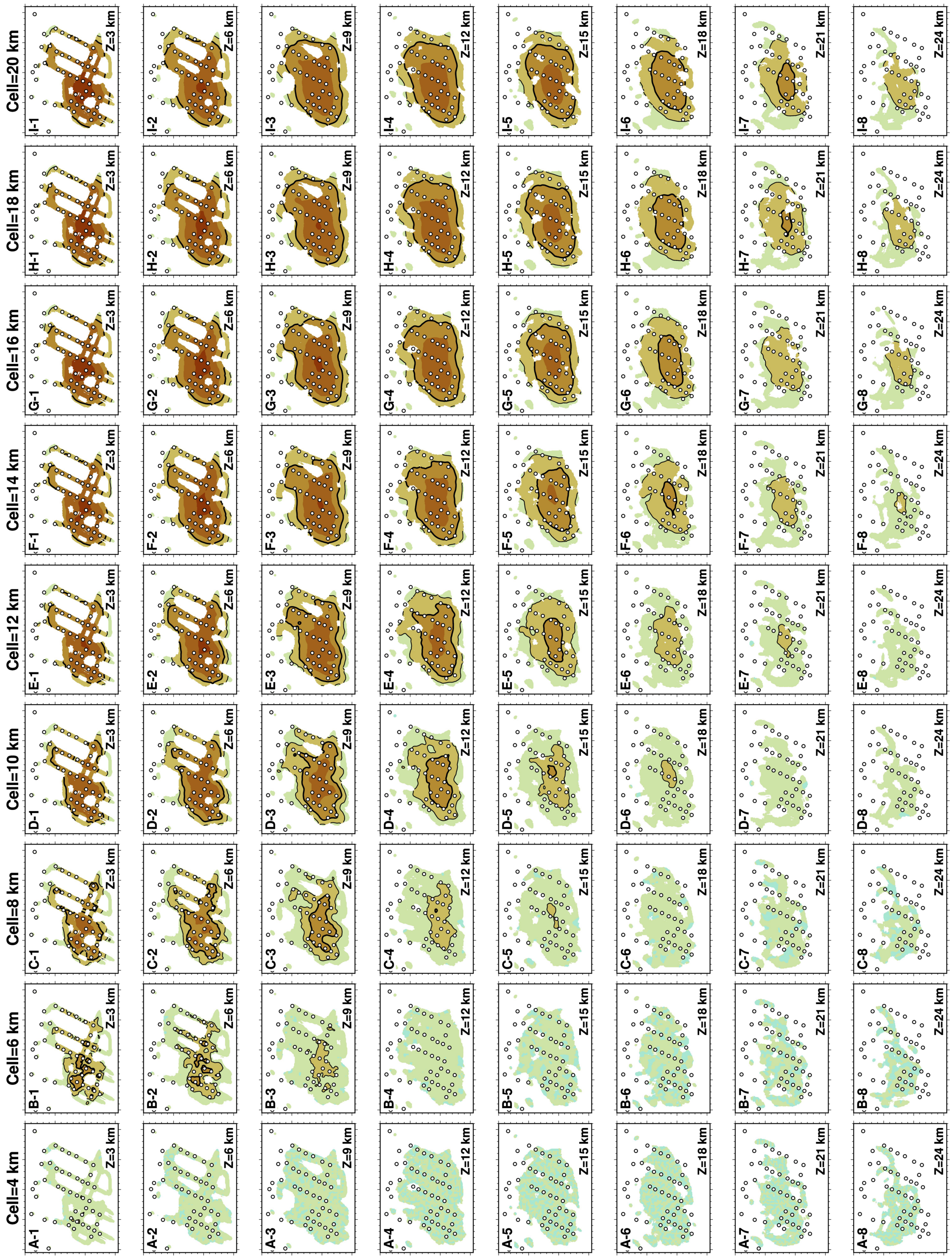

Figure S 14. **Averaged semblance of 8 checkerboard patterns for cell sizes of 4 to 20 km.** Contours of the semblance of 0.6 (thin line) and 0.7 (thick line) are plotted.

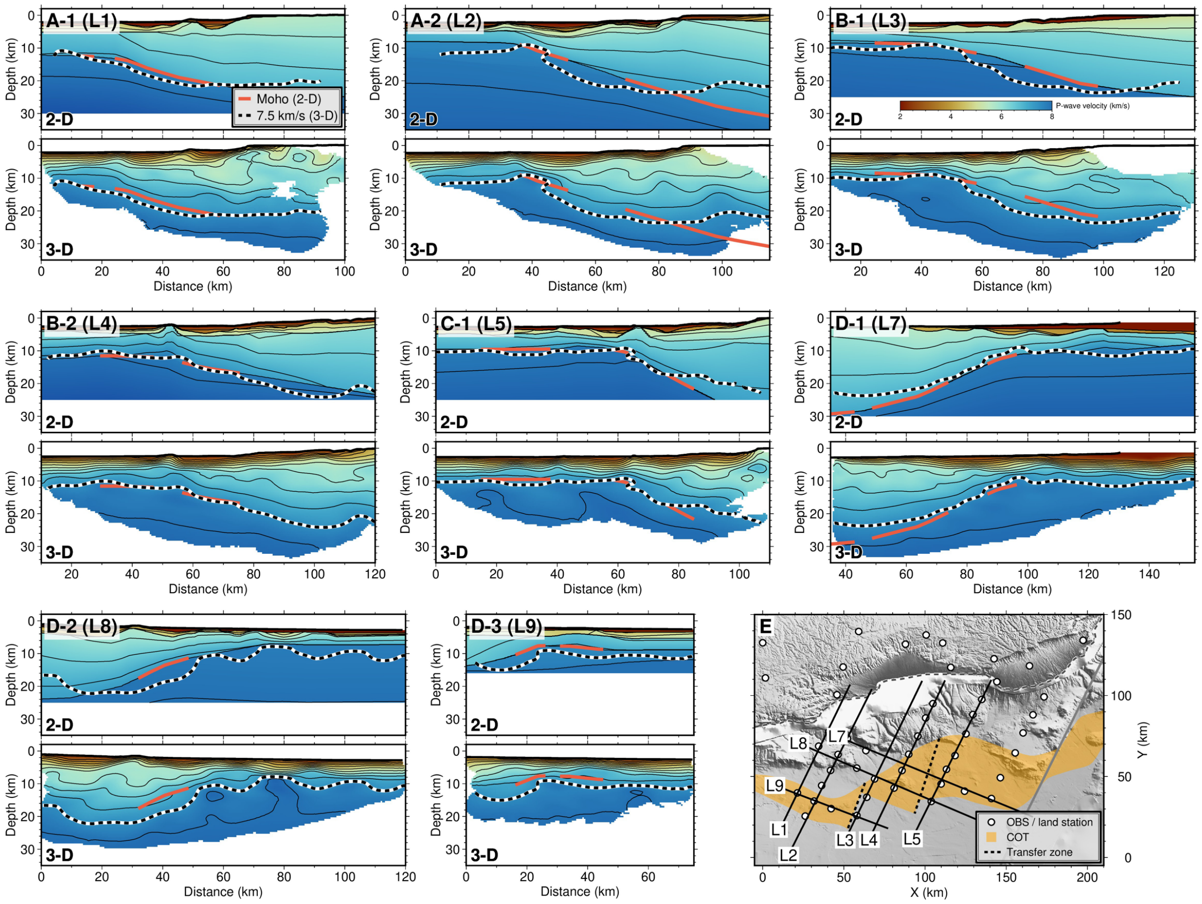

Figure S 15. **Comparison of previous 2-D (upper panels) and 3-D (lower panels) Vp models.** Red lines are Moho interfaces built with PmP reflections by 2-D Vp models using Ranvir algorithm (Leroy et al., 2010; Watremez et al., 2011). Contour interval is 0.5 km/s. Dashed lines are 7.5 km/s iso-velocities from our 3-D Vp models.

Range of shot-receiver offset (km)	Assigned uncertainty to traveltime picks (ms)
0-5	20
5-10	50
10-20	80
20-50	100
>50	150

Table S 1. **Assigned uncertainty for the FAST inversion model.**

Inversion parameter	Value
No. iteration	10
Lambda (λ)	6
Lambda0 (λ0)	100
Lambda reduction factor	1.414
Alpha (α)	0.95
Smoothness factor (sz)	0.125
Model dimensions - X×Y×Z	215×155×74 km
Forward spacing - horizontal	0.5 km
Forward spacing - vertical	0.5 km
Inversion spacing - horizontal	1 km
Inversion spacing - vertical	0.5 km

Table S 2. **Summary of inversion parameters for the FAST inversion model.**

Parameter	Minimum	Maximum	Example (Fig. S3)	unit
Velocity at the continental surface	3.5	4.5	4	km/s
Velocity at the seafloor	1.5	2	1.6	km/s
Velocity at the basement top	3.5	4.5	4	km/s
Velocity of the mantle	7.0	8.0	7.5	km/s
Thickness of the oceanic crust	4.0	8.0	6	km
Thickness of the upper mantle	1.5	4.5	3	km
∆Y	50	100	90	km
∆Z	5	20	15	km
Shift of continent-ocean boundary	-10 (south)	10 (north)	0	km

Table S 3. **Parameters of the starting model used in the Monte-Carlo analysis.**

References

Autin, J., Leroy, S., Beslier, M. O., d'Acremont, E., Razin, P., Ribodetti, A., et al. (2010). Continental break-up history of a deep magma-poor margin based on seismic reflection data (northeastern Gulf of Aden margin, offshore Oman). *Geophysical Journal International*, *180*(2), 501–519. https://doi.org/10.1111/j.1365-246X.2009.04424.x

Corbalán, A., Nedimović, M. R., Louden, K. E., Cannat, M., Grevemeyer, I., Watremez, L., & Leroy, S. (2021). Seismic Velocity Structure Along and Across the Ultraslow-Spreading Southwest Indian Ridge at 64°30′E Showcases Flipping Detachment Faults. *Journal of Geophysical Research: Solid Earth*, *126*(10), e2021JB022177. https://doi.org/10.1029/2021JB022177

d'Acremont, E., Leroy, S., Beslier, M. O., Bellahsen, N., Fournier, M., Robin, C., et al. (2005). Structure and evolution of the eastern Gulf of Aden conjugate margins from seismic reflection data. *Geophysical Journal International*, *160*(3), 869–890. https://doi.org/10.1111/j.1365-246X.2005.02524.x

d'Acremont, E., Leroy, S., Maia, M., Gente, P., & Autin, J. (2010). Volcanism, jump and propagation on the Sheba ridge, eastern Gulf of Aden: Segmentation evolution and implications for oceanic accretion processes. *Geophysical Journal International*, *180*(2), 535–551. https://doi.org/10.1111/j.1365-246X.2009.04448.x

Davy, R. G., Minshull, T. A., Bayrakci, G., Bull, J. M., Klaeschen, D., Papenberg, C., et al. (2016). Continental hyperextension, mantle exhumation, and thin oceanic crust at the continent-ocean transition, West Iberia: New insights from wide-angle seismic. *Journal of Geophysical Research: Solid Earth*, *121*(5), 3177–3199. https://doi.org/10.1002/2016JB012825

Korenaga, J., Holbrook, W. S., Kent, G. M., Kelemen, P. B., Detrick, R. S., Larsen, H. C., et al. (2000). Crustal structure of the southeast Greenland margin from joint refraction and reflection seismic tomography. *Journal of Geophysical Research: Solid Earth*, *105*(B9), 21591–21614. https://doi.org/10.1029/2000jb900188

Leroy, S. (2006). ENCENS cruise, RV L'Atalante. https://doi.org/10.17600/6010030

Leroy, S., Lucazeau, F., d'Acremont, E., Watremez, L., Autin, J., Rouzo, S., et al. (2010). Contrasted styles of rifting in the eastern Gulf of Aden: A combined wide-angle, multichannel seismic, and heat flow survey. *Geochemistry, Geophysics, Geosystems*, *11*(7), n/a-n/a. https://doi.org/10.1029/2009GC002963

Momoh, E., Cannat, M., Watremez, L., Leroy, S., & Singh, S. C. (2017). Quasi-3-D Seismic Reflection Imaging and Wide-Angle Velocity Structure of Nearly Amagmatic Oceanic Lithosphere at the Ultraslow-Spreading Southwest Indian Ridge. *Journal of Geophysical Research: Solid Earth*, *122*(12), 9511–9533. https://doi.org/10.1002/2017JB014754

Watremez, L., Leroy, S., Rouzo, S., d'Acremont, E., Unternehr, P., Ebinger, C., et al. (2011). The crustal structure of the north-eastern Gulf of Aden continental margin: Insights from wide-angle seismic data. *Geophysical Journal International*, *184*(2), 575–594. https://doi.org/10.1111/j.1365-246X.2010.04881.x

Watremez, L., Helen Lau, K. W., Nedimovic, M. R., & Louden, K. E. (2015). Traveltime tomography of a dense wide-angle profile across Orphan Basin. *Geophysics*, *80*(3), B69–B82. https://doi.org/10.1190/geo2014-0377.1

Weatherall, P., Marks, K. M., Jakobsson, M., Schmitt, T., Tani, S., Arndt, J. E., et al. (2015). A new digital bathymetric model of the world's oceans. *Earth and Space Science*, *2*(8), 331–345. https://doi.org/10.1002/2015EA000107

White, R. S., McKenzie, D., & O'Nions, R. K. (1992). Oceanic crustal thickness from seismic measurements and rare earth element inversions. *Journal of Geophysical Research*, *97*(B13). https://doi.org/10.1029/92jb01749

Zelt, C. A. (1998). Lateral velocity resolution from three-dimensional seismic refraction data. *Geophysical Journal International*, *135*(3), 1101–1112. https://doi.org/10.1046/j.1365-246X.1998.00695.x

Zelt, C. A., & Barton, P. J. (1998). Three-dimensional seismic refraction tomography: A comparison of two methods applied to data from the Faeroe Basin. *Journal of Geophysical Research: Solid Earth*, *103*(B4), 7187–7210. https://doi.org/10.1029/97JB03536

Zhang, J., & Toksöz, M. N. (1998). Nonlinear refraction traveltime tomography. *Geophysics*, *63*(5), 1726–1737. https://doi.org/10.1190/1.1444468